Journal of Physics G:
Nuclear and Particle
Physics

PAPER • **OPEN ACCESS**

Nuclear cross-section of the ^{nat}Eu(α, x) reactions up to 65 MeV: focus on the production of theranostic radioisotopes of terbium

To cite this article: Michele Colucci *et al* 2025 *J. Phys. G: Nucl. Part. Phys.* **52** 115102

OPEN ACCESS
IOP Publishing
Journal of Physics G: Nuclear and Particle Physics
J. Phys. G: Nucl. Part. Phys. **52** (2025) 115102 (32pp)
https://doi.org/10.1088/1361-6471/ae1627

Nuclear cross-section of the ^{nat}Eu(α, *x*) reactions up to 65 MeV: focus on the production of theranostic radioisotopes of terbium

Michele Colucci[1,*], Etienne Nigron[2], Ferid Haddad[2,3], Arnaud Guertin[3], Eugenio Gibertini[4], Luca Magagnin[4], Flavia Maria Groppi Garlandini[1] and Simone Manenti[1]

[1] LASA Laboratory, Department of Physics—La Statale, University of Milan and INFN section of Milan, Segrate, Milan, Italy
[2] GIP Arronax, Saint-Herblain, Nantes, France
[3] Laboratoire Subatech, IN2P3-CNRS, IMT Atlantique, Nantes Université, Nantes, France
[4] Department of Chemistry, Materials and Chemical Engineering 'Giulio Natta', Politecnico di Milano, Milan, Italy

E-mail: michele.colucci@unimi.it

Received 21 July 2025, revised 26 September 2025
Accepted for publication 22 October 2025
Published 13 November 2025

Abstract

Terbium is considered a promising element for theranostic applications in nuclear medicine due to its four medically-relevant radioisotopes: ^{149}Tb, ^{152}Tb, ^{155}Tb and ^{161}Tb, each suited for different diagnostic or therapeutic uses. Despite its potential, the clinical adoption of terbium is hindered by the lack of large-scale production methods for these isotopes. This work presents the first comprehensive study of nuclear cross-sections for ^{nat}Eu(α, *x*) reactions, using europium oxide targets, in the energy range of 20–65 MeV for ^{155}Tb production. Theoretical simulations using TALYS 1.96 were performed, highlighting the need for further model refinements. Additionally, we employed the Non-dominated Sorting Genetic algorithm II (NSGA-II) to optimize the production parameters for ^{155}Tb on enriched ^{153}Eu targets.These findings contribute to optimizing production routes for terbium isotopes, supporting future developments in nuclear medicine.

* Author to whom any correspondence should be addressed.

Keywords: cross-section, terbium, terbium-155, theranostic, alpha beams, Eu target, NSGA-II

1. Introduction

Terbium is a promising theranostic element as it presents four radionuclides with potential applications in nuclear medicine, namely ^{149}Tb, ^{152}Tb, ^{155}Tb and ^{161}Tb [1].

^{149}Tb ($I_{\alpha} = 16.7\%$, $I_{ec,\beta^+} = 83.3\%$, $T_{1/2} = 4.118$ h [2]) has been suggested for the purpose of targeted alpha therapy together with its potential application in PET analysis of the radiopharmaceutical distribution due to the complementary β^+-decay [3]. ^{152}Tb ($I_{ec,\beta^+} = 100\%$, $T_{1/2} = 17.5$ h [2]) has suitable physical characteristics for PET imaging in pre-treatment dosimetry of radiolanthanides therapy [4, 5]. ^{155}Tb ($I_{ec} = 100\%$, $T_{1/2} = 5.32$ d [2]) has been suggested for SPECT studies [6] due to his γ-rays emissions ($E_{\gamma} = 105.305$ keV and $E_{\gamma} = 86.545$ keV [2]), while the emission of Auger electrons open the possibility to use this radionuclide as a therapeutic agent. ^{161}Tb ($I_{\beta^-} = 100\%$, $T_{1/2} = 6.89$ d [2]) presents an intense emission of low energy Auger and conversion electrons that happens to have a high therapeutic potential due to their high LET [7]. The presence of low energy γ-rays ($E_{\gamma} = 74.567\,11$ keV $I_{\gamma} = 10.2\%$ [2]) makes it possible to perform SPECT acquisition during the therapy [8]. Thus, terbium is a theranostic element, considering the possibility to use these set of radionuclides for both diagnosis and therapy.

The main limit to the spread of terbium in the clinical practice, apart from ^{161}Tb, is the unavailability of a production process at large scale of these radionuclides. Many different reactions induced by light ions (protons, deuterons and alpha particles) on different targets have been investigated, including natural gadolinium [9–13] or enriched gadolinium (^{152}Gd [14], ^{155}Gd [12, 15–18], ^{156}Gd [12, 16, 17], ^{160}Gd [19]), natural dysprosium [20, 21], enriched ^{151}Eu [22, 23] and very recently on enriched ^{153}Eu [24]. The use of ISOL technique lead to the production of pure terbium isotopes, but limited quantities can be produced and only few centers worldwide have the required instrumentation, preventing the spread of the clinical use of terbium. Extensive reviews of the production methods may be found in literature [13, 25–27].

In this study, cross-sections of nuclear reactions induced by α-particles on natural europium targets are measured for the first time. A discussion regarding the optimization of the production of ^{155}Tb on enriched ^{153}Eu targets is presented.

2. Experimentals

The cross-sections of the ^{nat}Eu(α, x) nuclear reactions have been determined across an energy range spanning from 20 to 65 MeV, employing the stacked-foils technique. Four distinct stacks were assembled, each housing 4–5 europium foils, whose fabrication is described in section 2.1. Accompanying, there were 50 μm kapton foils serving as catchers before the europium foil so prevent eventual loss of powder during the irradiation and the measurements, alongside with aluminum (purity >99.0%) and copper foils (purity >99.95%) (Goodfellow Cambridge Ltd., Ermine Business Park, Huntingdon, England) of various thicknesses played dual roles, monitors and energy degraders within the experimental setup.

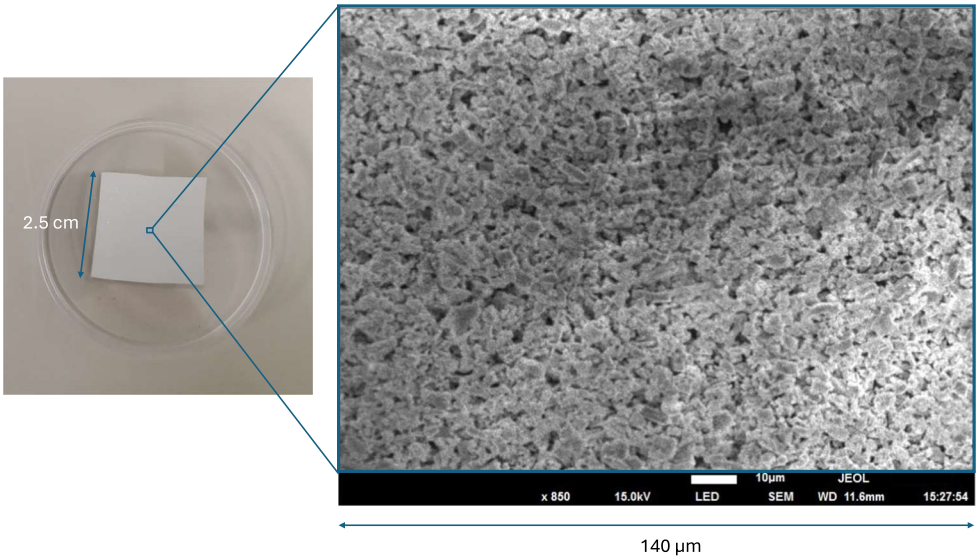

Figure 1. Example of our $^{nat}Eu_2O_3$ target. (left) Picture of one of the targets. (right) SEM acquisition of a portion of the sample. The nanoparticles of $^{nat}Eu_2O_3$ are clearly visible. The target results uniform at the scale of interest.

2.1. Europium target preparation and characterization

Europium oxide ($^{nat}Eu_2O_3$) targets were prepared by blade coating of a slurry containing $^{nat}Eu_2O_3$ nanopowder (purity >99.995%—Nanografi Nano Technology, Germany) and Na-CMC (TCI Chemicals) as binder. Typically, 7.44 g of a 2.5% wt. Na-CMC aqueous solution were added to a ball-milling zirconium oxide jar (50 ml capacity) along with 7.4 ml of water, 6 g of $^{nat}Eu_2O_3$ particles and 6 zirconium oxide spheres. A homogeneous slurry was obtained by ball-milling at 200 rpm in a planetary ball milling (TOB New Energy) for 2 h. The viscous slurry was uniformly coated on Al foil by blade coating at 100 µm wet thickness, room dried for few h and finally overnight dried in vacuum at 70 °C.

$^{nat}Eu_2O_3$ distribution was observed by JEOL JSM 71OOF scanning electron microscope (SEM) with a magnification of 850× at 15 kV acceleration voltage. At the scale of interest for the irradiation (beam diameter of 1 cm) the target resulted uniform as it can be seen in figure 1.

The precise mass amount of europium present in the sample has been determined with the Thermo Scientific iCAP 6000 Series Inductively Coupled Plasma—Atomic Emission Spectroscopy (ICP-AES). A mass of 1.56 ± 0.01 mg of powder was scratched from the surface of a non irradiated targets and dissolved in 6 ml of 5 M HNO_3 and diluted to avoid saturation of the instrumentation. The percentage in mass of europium was obtained to be $m_{Eu\%} = (78 \pm 2)\%$ of the total mass of powder deposited on the targets. This value has been assumed to be the same for all targets, as they were all produced together from the same mixture of europium oxide powder and Na-CMC aqueous solution.

2.2. Irradiation setup

Irradiations were executed using the high-intensity cyclotron (IBA-C70XP, $K = 70$) at the GIP ARRONAX research center in Saint-Herblain (FR) [28]. Employing a $^4He^{2+}$ beam with

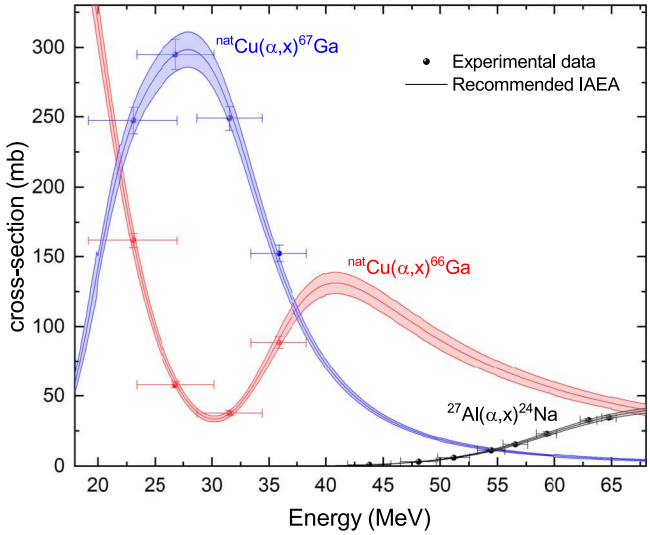

Figure 2. Comparison of experimental cross sections for monitor reactions, ^{nat}Al(α, x)^{24}Na (black points), ^{nat}Cu(α, x)^{67}Ga (blue points), and ^{nat}Cu(α, x)^{66}Ga (red points), with IAEA-recommended values (black, blue, and red lines, respectively) [30]. The shaded bands around the curves indicate the one-standard-deviation uncertainty in the recommended values.

a fixed energy of 67.5 ± 0.5 MeV, different entrance energies on the stack were achieved by introducing thick aluminum foils in front of the stack. The stacks were positioned at a distance of 5 cm from the 50 μm kapton exit window of the cyclotron beam line. The shape and position of the beam were meticulously verified when tuning the beam by irradiating an Al_2O_3 scintillating foil. The energy of the beam impinging on each target of the stack was determined using SRIM software [29].

A total of four irradiation sessions over a period of 4 months were conducted on 18 natural europium targets, spanning an energy interval from 20 to 65 MeV. Each session maintained a constant current of approximately 100 nA for a duration of 1 h. The selection of degrader thickness ensured overlap in the energy range between irradiation sessions. Throughout the irradiation process, beam current stability was closely monitored using an instrumented beam dump in conjunction with a current integrator. Verification of integrated charge and beam energy was performed by comparing experimental cross-sections of monitor reactions (^{nat}Al(α, x)^{24}Na, ^{nat}Cu(α, x)^{66}Ga and ^{nat}Cu(α, x)^{67}Ga) with IAEA-recommended values [30]. The comparison is reported in figure 2, where an excellent agreement between the experimental data (points) and the recommended curves (lines) can be noted.

2.3. Measurements

Activity measurements have been performed approximately 1 h after the irradiation, and in any case after the time needed to keep the dead time lower than 5%. Measurements have been repeated continuously for 2 weeks after each irradiation to reduce the uncertainty of the result and to follow the decay of each radionuclide. Short term gamma spectrometry measurements were performed at GIP ARRONAX using two Canberra HPGe detectors (n-type) calibrated using certified point sources of ^{152}Eu and ^{241}Am (LEA-CERCA, France). The first source permits to calibrate the detectors in the 121.8–1408.0 keV energy range, while the latter permits to calibrate at lower energy using the peaks at 26.3 keV (2.27%) and at

Table 1. List of detected radionuclides: symbol, decay mode, half-life, gamma emissions used to determine the activities alongside their characteristics [2], and production reactions involved. Peaks labeled '*a*' are combined in a single peak with intensity equal to the sum of the intensities and as energy the average energy weighted for the intensity, while peaks labeled with * are peaks with superposition with others radionuclides. Uncertainties on E_γ and I_γ values are italicized and pertain to the last significant figures.

Nuclide	$T_{1/2}$	E_γ (keV)	I_γ (%)	Contributing Reactions	E_{th} (MeV)
^{156g}Tb	5.35 d	534.29 6	67 6	^{153}Eu(α, n)	9.09
e.c., β^+ 100%	—	1065.11 15	10.8 10	^{156m1}Tb (IT)	—
	—	—	—	^{156m2}Tb (IT)	—
^{155}Tb	5.32 d	105.318 3	25.1 13	^{153}Eu(α, 2n)	16.13
e.c., 100%	—	—	—	—	—
^{154m2}Tb	22.7 h	346.70 4*	69 7	^{151}Eu(α, n)	10.33
e.c., β^+ 98.2%	—	722.5 1*	1.1 4	^{153}Eu(α, 3n)	25.46
IT 1.8%	—	873.21 4*	3.4 4		
^{154m1}Tb	9.4 h	346.70 4*	1.6 3	^{151}Eu(α, n)	10.33
e.c., β^+ 78.2%	—	540.18 6	20 3	^{153}Eu(α, 3n)	25.46
IT 21.8%	—	722.5 1*	0.37 11	—	—
	—	873.21 4*	9.2 16	—	—
^{154g}Tb	21.5 h	722.12 8*	7.7 6	^{151}Eu(α, n)	10.33
e.c., β^+ 100%	—	873.21 4*	5.3 5	^{153}Eu(α, 3n)	25.46
	—	—	—	^{154m1}Tb (IT)	—
	—	—	—	^{154m2}Tb (IT)	—
^{153}Tb	2.34 d	212.00 2	28.5 19	^{151}Eu(α, 2n)	17.38
e.c., β^+ 100%	—	—	—	^{153}Eu(α, 4n)	32.51
^{152}Tb	17.5 h	411.1165 13	3.6 1	^{151}Eu(α, 3n)	26.23
e.c., β^+ 100%		764.89 7	2.74 7	^{153}Eu(α, 5n)	41.13
^{151}Tb	17.609 h	251.863^{a}10	26.3 11	^{151}Eu(α, 4n)	33.51
e.c., β^+ 99.9905%	—	252.3^{a}5	0.34 9	^{153}Eu(α, 6n)	48.63
α 0.0095%	—	252.4^{a}5	0.062 14	—	—
	—	287.357 1	28.3 12	—	—
	—	616.561 15	10.4 4	—	—
	—	731.2^{a}5	0.62 14	—	—
	—	731.227^{a}11	7.7 3	—	—
^{150}Tb	3.48 h	638.050 16	72 10	^{151}Eu(α, 5n)	42.26
e.c., β^+ 100%	—	—	—	^{153}Eu(α, 7n)	57.38
α 0.0007%	—	—	—	—	—
^{149}Tb	4.118 h	352.24 2	29.8 7	^{151}Eu(α, 6n)	50.10
e.c., β^+ 83.3%	—	—	—	^{153}Eu(α, 8n)	65.21
α 16.7%	—	—	—	—	—

Table 1. (Continued.)

Nuclide	$T_{1/2}$	E_γ (keV)	I_γ (%)	Contributing Reactions	E_{th} (MeV)
^{153g}Gd	240.4 d	97.43100 21	30.0 6	^{151}Eu(α, d)	12.72
e.c., 100%	—	103.18012 17	22.1 3	^{153}Eu(α, $n+t$)	21.47
	—	—	—	^{153}Tb (β^+, 100%)	—
	—	—	—	^{153m1}Gd (IT, 100%)	—
	—	—	—	^{153m2}Gd (IT, 100%)	—
^{151}Gd	123.9 d	153.60 1	6.2 4	^{151}Eu(α, $n+t$)	21.46
e.c., 100%	—	174.70 1	2.96 20	^{153}Eu(α, $3n+t$)	36.59
	—	243.29 3	5.6 4	^{151m}Tb (β^+, 6.6%)	—
	—	307.50 1	1.04 7	^{151}Tb (β^+, 99.99%)	—
^{149}Gd	9.28 d	149.730 10	48.4 26	^{151}Eu(α, $3n+t$)	36.95
e.c., β^+ 100%	—	298.633 5	27.9 15	^{153}Eu(α, $5n+t$)	52.07
	—	346.650*10	23.7 13	^{149}Tb (β^+, 83.3%)	—
	—	—	—	^{149m}Tb (β^+, 99.98%)	—
^{149}Eu	93.1 d	277.089 10	4.18 4	^{151}Eu (α, $\alpha+2n$)	14.63
e.c., 100%		327.526 10	4.75 5	^{153}Eu (α, $\alpha+4n$)	29.75
	—	—	—	^{149}Gd (β^+, 100%)	—
^{148}Eu	54.5 d	550.284[a]12	99 3	^{151}Eu (α, $\alpha+3n$)	38.12
e.c., β^+ 100%	—	553.231[a]14	12.9 22	^{153}Eu (α, $\alpha+5n$)	23.00
	—	553.260[a]15	5.0 22	^{148m}Eu (IT, 100%)	—
	—	629.987 8	71.9 22	—	—

59.5 keV (35.9%). Moreover, after 3 months, the measurements continued at LASA laboratory (Segrate, MI) to determine the activity of produced long lived radionuclides. In this case three ORTEC HPGe detectors (p-type) calibrated with two point-like sources of ^{152}Eu and ^{133}Ba (LEA-CERCA, France) were employed. Both calibration and activity measurements were performed in the same geometry, with the source–detector distance always kept larger than 19 cm in order to minimize true-coincidence summing effects.

The list of radionuclides of which the cross-section has been determined is reported in table 1 alongside with their nuclear properties, the gamma rays used to determine the activity, the nuclear reactions involved in the production and the respective threshold energy [2].

Table 2. Cross-sections of the ^{nat}Eu(α, xn)^{1xx}Tb nuclear reactions (Part 1). The cross-sections are expressed in mb.

$E \pm \Delta E$ (MeV)	^{156g,cum}Tb	^{155}Tb	^{154m2}Tb	^{154m1}Tb	^{154g}Tb
21 ± 4	52 ± 3	259 ± 8	8.4 ± 0.8	122 ± 5	29 ± 5
25 ± 4	18.2 ± 1.0	520 ± 20	3.8 ± 0.3	43 ± 2	11 ± 3
28 ± 3	11.0 ± 1.0	560 ± 20	13.1 ± 1.1	144 ± 14	37 ± 5
33 ± 3	6.5 ± 0.8	182 ± 8	51 ± 5	560 ± 40	98 ± 11
36 ± 3	5.4 ± 0.7	118 ± 5	66 ± 5	680 ± 30	125 ± 20
37 ± 2	5.3 ± 0.6	81 ± 5	73 ± 6	790 ± 30	124 ± 15
39 ± 2	4.6 ± 0.8	60 ± 5	66 ± 4	700 ± 30	127 ± 20
42 ± 2	3.6 ± 0.2	45.3 ± 1.8	56 ± 3	620 ± 40	99 ± 14
44.2 ± 1.9	2.8 ± 0.5	34 ± 2	38 ± 3	412 ± 16	77 ± 7
46.2 ± 1.7	2.1 ± 0.6	35 ± 2	30 ± 3	330 ± 30	62 ± 13
48.5 ± 1.6	2.6 ± 0.4	24.7 ± 1.1	18.1 ± 1.3	203 ± 18	29 ± 6
51.5 ± 1.4	2.4 ± 0.6	24.9 ± 0.8	14.5 ± 1.3	141 ± 14	15 ± 7
54.8 ± 1.2	2.1 ± 0.7	17.6 ± 1.0	9.3 ± 0.8	94 ± 9	19 ± 6
56.9 ± 1.1	2.2 ± 0.7	16.4 ± 1.1	8.2 ± 1.5	79 ± 8	16 ± 4
59.6 ± 0.9	2.2 ± 0.5	13.2 ± 0.4	8.1 ± 0.7	68 ± 6	12 ± 4
61.5 ± 0.8	2.1 ± 0.7	11 ± 2	8.2 ± 1.4	61 ± 6	13 ± 5
63.3 ± 0.7	3.1 ± 0.3	10.6 ± 1.0	7.3 ± 1.0	54 ± 6	13 ± 5
65.1 ± 0.6	3.3 ± 0.4	11.1 ± 0.8	5.5 ± 1.0	46 ± 5	10 ± 4

3. Results

The production cross-sections $\sigma(E)$ (mb) were determined using the following expression:

$$\sigma(E) = \frac{M \cdot Ze}{\lambda \cdot N_A \cdot \rho x \cdot m_{Eu\%} \cdot Q} \cdot \frac{C}{LT \cdot \varepsilon \cdot I_\gamma} \cdot e^{\lambda t_{dec}} \cdot D(RT) \cdot G(t_{irr}) \cdot 10^{27} \quad (1)$$

Here, E (MeV) represents the mean alpha beam energy within the target foil, C is the net count at the photo-peak energy E_γ, ε is the detector efficiency calculated at energy E_γ, I_γ denotes the gamma emission probability at energy E_γ, LT (s) is the live time of the measurement and $m_{Eu\%}$ is the percentage in mass of Eu within the target. The term RT (s) is the real time of the measurement (comprising LT and the dead time). M stands for the atomic mass (in g mol^{-1}) of europium, Ze is the alpha particle charge (C), λ is the decay constant (s^{-1}) of the measured radionuclide, and Q refers to the total incident alpha beam charge (C). Furthermore, N_A is Avogadro's constant (mol^{-1}), t_{irr} (s) represents the irradiation time, and t_{dec} (s) is the delay time between the End Of Bombardment (EOB) and the start of the measurements. Two multiplicative factors are applied: the growth factor $G(t_{irr})$, which accounts for the decay of the produced radionuclide during irradiation, and the decay factor $D(RT)$, which considers the decay during the measurement period [31]. The mass thickness ρx (g cm^{-2}) is calculated as the ratio of the target's mass to its surface area. The mass is measured using a precision scale with a sensitivity of 10^{-5} g, while the surface area is determined by measuring the length of the square target's sides with a caliper having a sensitivity of 10^{-2} mm.

The experimental cross-section values, are reported in tables 2, 3, 4 and 5. The excitation functions are presented in figures 3–22. In the same figures, the curves obtained with TALYS

Table 3. Cross-sections of the $^{nat}Eu(\alpha, xn)^{1xx}Tb$ nuclear reactions (Part 2). The cross-sections are expressed in mb.

$E \pm \Delta E$ (MeV)	^{153}Tb	^{152}Tb	^{151}Tb	^{150}Tb	^{149}Tb
21 ± 4	183 ± 6	—	—	—	—
25 ± 4	474 ± 18	—	—	—	—
28 ± 3	600 ± 20	44 ± 5	—	—	—
33 ± 3	286 ± 10	352 ± 18	—	—	—
36 ± 3	193 ± 7	509 ± 17	—	—	—
37 ± 2	154 ± 6	—	9 ± 2	—	—
39 ± 2	166 ± 6	560 ± 30	29 ± 2	—	—
42 ± 2	307 ± 11	530 ± 30	121 ± 12	—	—
44.2 ± 1.9	489 ± 18	410 ± 11	276 ± 11	—	—
46.2 ± 1.7	678 ± 11	350 ± 15	413 ± 11	—	—
48.5 ± 1.6	710 ± 30	237 ± 14	511 ± 18	6.0 ± 1.1	—
51.5 ± 1.4	746 ± 9	267 ± 15	580 ± 12	21.6 ± 1.4	—
54.8 ± 1.2	553 ± 9	375 ± 10	471 ± 18	41.2 ± 1.9	—
56.9 ± 1.1	435 ± 19	510 ± 30	391 ± 15	48 ± 2	—
59.6 ± 0.9	317 ± 9	578 ± 19	315 ± 11	56.5 ± 1.4	3.9 ± 0.5
61.5 ± 0.8	242 ± 11	580 ± 25	280 ± 13	50 ± 2	6.0 ± 0.6
63.3 ± 0.7	193 ± 3	560 ± 30	275 ± 12	43.8 ± 1.1	7.2 ± 0.8
65.1 ± 0.6	149 ± 17	520 ± 20	301 ± 16	37.7 ± 1.7	9.6 ± 1.0

Table 4. Cross-sections of the $^{nat}Eu(\alpha,x)^{1xx}Gd$ and ^{1xx}Eu nuclear reactions. The cross-sections are expressed in mb.

$E \pm \Delta E$ (MeV)	$^{153g,cum}Gd$	$^{151,cum}Gd$	$^{149,cum}Gd$	$^{149,cum}Eu$	^{148}Eu
21 ± 4	192 ± 4	—	—	—	—
25 ± 4	492 ± 8	—	—	—	—
28 ± 3	621 ± 11	—	—	—	—
33 ± 3	314 ± 6	2.0 ± 0.2	—	2.1 ± 0.5	—
36 ± 3	221 ± 5	—	—	7 ± 3	—
37 ± 2	185 ± 4	9.6 ± 0.7	—	5.3 ± 0.2	—
39 ± 2	195 ± 5	30.9 ± 1.1	—	6.4 ± 0.5	—
42 ± 2	341 ± 5	124 ± 3	—	9.9 ± 1.3	0.5 ± 0.2
44.2 ± 1.9	531 ± 11	251 ± 4	—	17 ± 3	2.2 ± 0.3
46.2 ± 1.7	746 ± 12	407 ± 7	—	22.0 ± 0.9	4.7 ± 0.3
48.5 ± 1.6	757 ± 14	493 ± 12	—	25 ± 3	9.7 ± 0.2
51.5 ± 1.4	853 ± 16	594 ± 15	—	22 ± 3	18.8 ± 0.7
54.8 ± 1.2	655 ± 8	504 ± 11	—	26 ± 6	25.4 ± 0.5
56.9 ± 1.1	542 ± 10	437 ± 7	2.7 ± 0.3	32 ± 9	27.9 ± 0.2
59.6 ± 0.9	418 ± 8	369 ± 7	11.8 ± 0.4	52 ± 7	29.5 ± 0.8
61.5 ± 0.8	341 ± 2	343 ± 8	31.4 ± 1.6	66 ± 4	27.7 ± 0.5
63.3 ± 0.7	299 ± 6	344 ± 11	63 ± 4	103 ± 11	27.7 ± 0.6
65.1 ± 0.6	264 ± 3	374 ± 5	107 ± 3	146 ± 11	27.2 ± 0.5

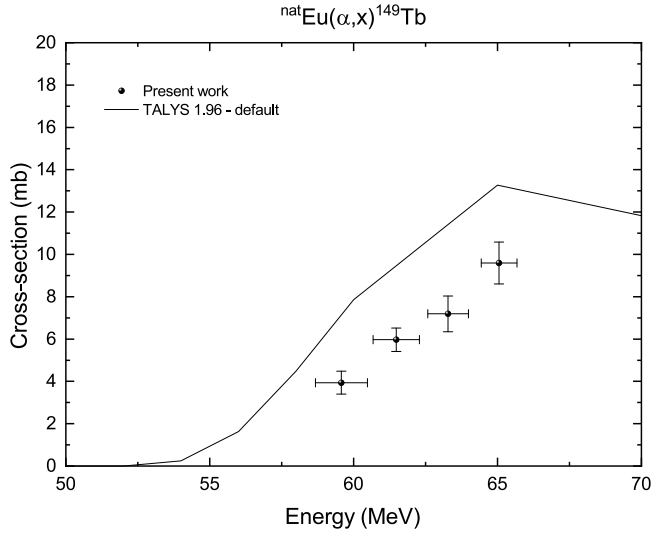

Figure 3. Cross-section for the ^{nat}Eu(α, x)^{149}Tb reaction. The curve obtained with TALYS 1.96 nuclear code run with default options are compared with the experimental results.

Table 5. Independent cross-sections of the ^{nat}Eu(α, x)^{153,151,149}Gd^{ind} and ^{149}Eu^{ind} nuclear reactions. The cross-sections are expressed in mb.

$E \pm \Delta E$ (MeV)	^{153g}Gd^{ind}	^{151}Gd^{ind}	^{149}Gd^{ind}	^{149}Eu^{ind}
33 ± 3	26 ± 12	—	—	2.1 ± 0.5
36 ± 3	26 ± 8	—	—	7 ± 3
37 ± 2	29 ± 8	—	—	5.3 ± 0.2
39 ± 2	27 ± 8	—	—	6.4 ± 0.5
42 ± 2	31 ± 12	—	—	9.9 ± 1.3
44.2 ± 1.9	38 ± 21	—	—	17 ± 3
46.2 ± 1.7	62 ± 16	—	—	22.0 ± 0.9
48.5 ± 1.6	40 ± 29	—	—	25 ± 3
51.5 ± 1.4	100 ± 18	—	—	22 ± 3
54.8 ± 1.2	96 ± 12	29 ± 21	—	26 ± 6
56.9 ± 1.1	100 ± 20	44 ± 16	2.7 ± 0.3	29 ± 9
59.6 ± 0.9	98 ± 12	52 ± 13	8.5 ± 0.7	39 ± 7
61.5 ± 0.8	96 ± 11	61 ± 15	26.3 ± 1.7	32 ± 4
63.3 ± 0.7	104 ± 6	67 ± 17	57 ± 4	33 ± 11
65.1 ± 0.6	114 ± 17	72 ± 17	99 ± 3	28 ± 12

1.96 code [32, 33] ran with default settings are compared with the experimental data. A systematic energy shift of about 5 MeV between TALYS predictions and experimental data is observed, in agreement with the findings of Kormazeva *et al* [24], suggesting that future works should improve the level density and α-optical model parameters for a better theoretical description.

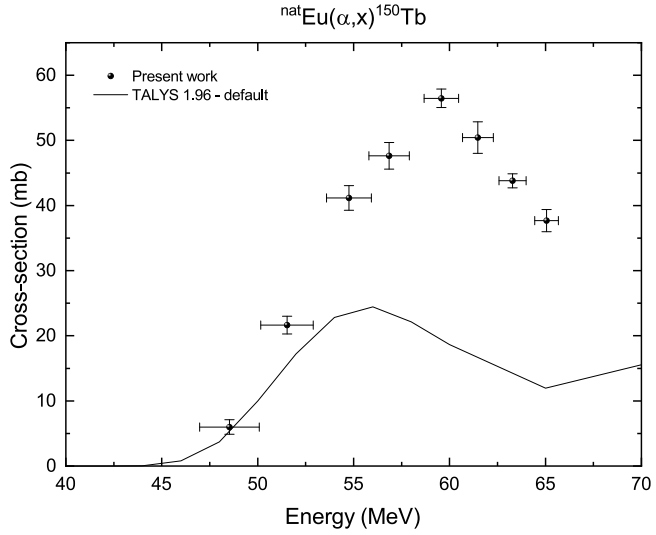

Figure 4. Cross-section for the ^{nat}Eu(α, x)^{150}Tb reaction. The curve obtained with TALYS 1.96 nuclear code run with default options are compared with the experimental results.

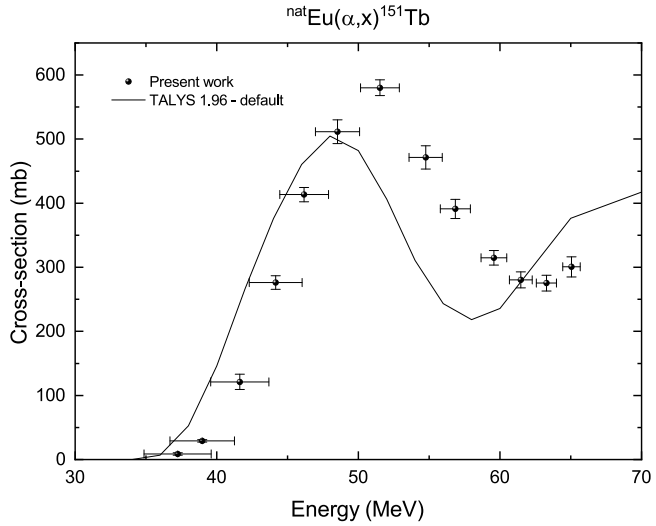

Figure 5. Cross-section for the ^{nat}Eu(α, x)^{151}Tb reaction. The curve obtained with TALYS 1.96 nuclear code run with default options are compared with the experimental results.

3.1. Uncertainty estimation for cross section measurements

The uncertainty associated with cross section measurements is evaluated by propagating the errors of the relevant physical quantities. The absolute uncertainty in the cross section, denoted as ϵ_σ, is calculated using the following expression:

$$\epsilon_\sigma = \sqrt{\left(\frac{\epsilon_A}{A}\right)^2 + \left(\frac{\epsilon_\rho}{\rho x}\right)^2 + \left(\frac{\epsilon_Q}{Q}\right)^2 + \left(\frac{\epsilon_{m_{\mathrm{Eu}\%}}}{m_{\mathrm{Eu}\%}}\right)^2} \cdot \sigma \tag{2}$$

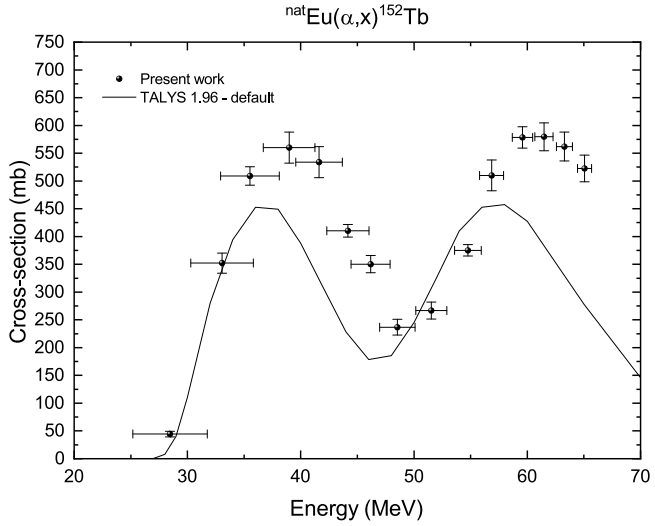

Figure 6. Cross-section for the ^{nat}Eu(α, x)^{152}Tb reaction. The curve obtained with TALYS 1.96 nuclear code run with default options are compared with the experimental results.

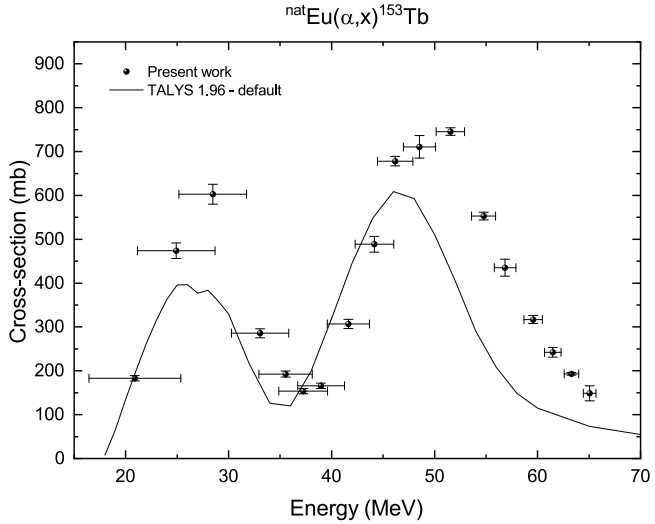

Figure 7. Cross-section for the ^{nat}Eu(α, x)^{153}Tb reaction. The curve obtained with TALYS 1.96 nuclear code run with default options are compared with the experimental results.

Here, ϵ_i represents the uncertainty associated with the quantity i. Specifically, the uncertainty in the activity A is computed via:

$$\epsilon_A = \sqrt{\left(\frac{\epsilon_{\mathrm{CPS}}}{\mathrm{CPS}}\right)^2 + \left(\frac{\epsilon_{I_\gamma}}{I_\gamma}\right)^2 + \left(\frac{\epsilon_\varepsilon}{\varepsilon}\right)^2} \cdot A \tag{3}$$

In this context, the count rate per second (CPS) is given by $\mathrm{CPS} = \frac{C}{LT}$, where C is the number of detected counts and LT is the live time. The uncertainty in the gamma emission

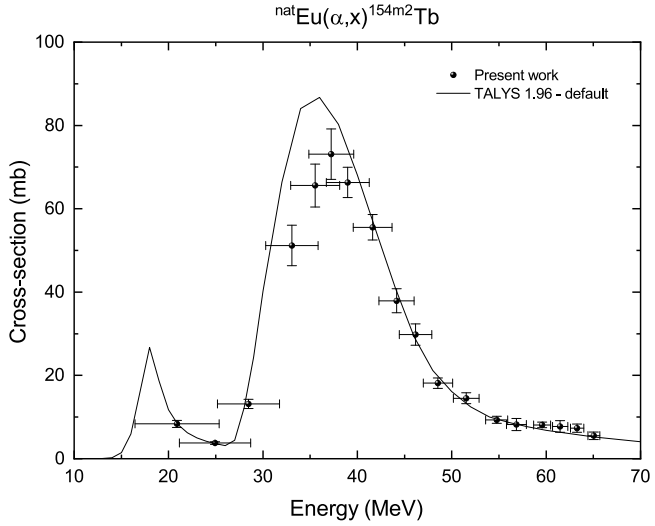

Figure 8. Cross-section for the $^{\text{nat}}\text{Eu}(\alpha, x)^{154\text{m2}}\text{Tb}$ reaction. The experimental data are compared with TALYS 1.96 nuclear code predictions.

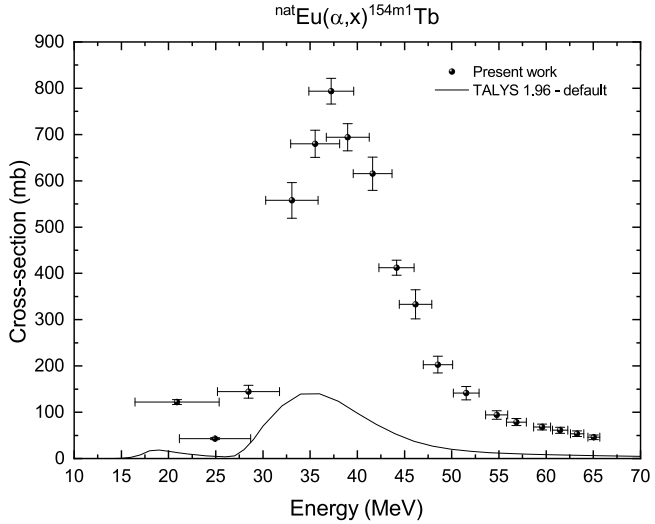

Figure 9. Cross-section for the $^{\text{nat}}\text{Eu}(\alpha, x)^{154\text{m1}}\text{Tb}$ reaction. Experimental data are compared with TALYS 1.96 nuclear code predictions.

probability I_γ is obtained from evaluated nuclear data libraries [2], and the detector efficiency uncertainty ϵ_ε is typically below 3%, varying with photon energy. The charge uncertainty ϵ_Q accounts for both measurement precision and systematic effects from reference data, such as those recommended by the IAEA [30].

Equation 2 assumes statistical independence of the contributing uncertainties. In practice, A and Q are both dependent on the detector efficiency (specifically through ε^{-1}) and are therefore expected to be positively correlated. This common dependence on ε^{-1} indicates

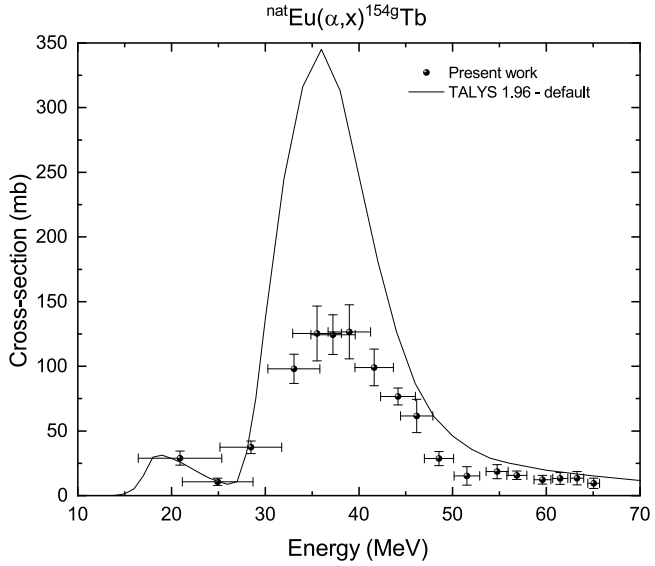

Figure 10. Cross-section for the ^{nat}Eu(α, x)^{154g}Tb reaction. Experimental data are compared with TALYS 1.96 nuclear code predictions.

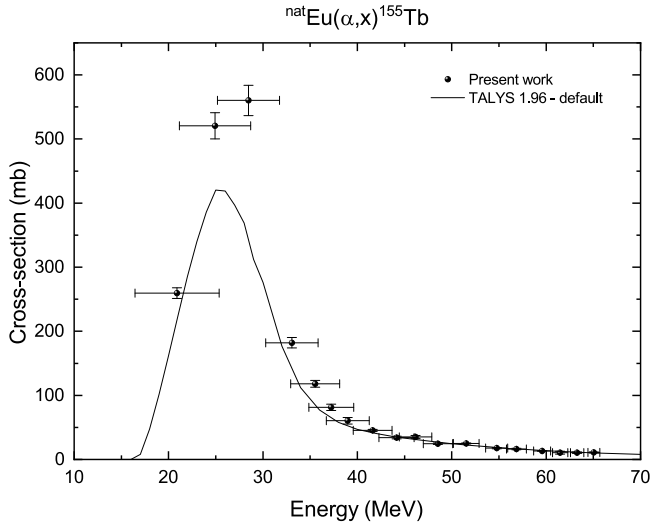

Figure 11. Cross-section for the ^{nat}Eu(α, x)^{155}Tb reaction. The curve obtained with TALYS 1.96 nuclear code run with default options are compared with the experimental results.

that their covariance is positive. Since in equation 1 the cross section scales as $\sigma \propto A/Q$, one has $\partial\sigma/\partial A > 0$ and $\partial\sigma/\partial Q < 0$. Accordingly, in the full error propagation the covariance term is negative and thus reduces the combined uncertainty. As our measurements did not provide paired determinations allowing a reliable estimate of the covariance, we set it to zero, which yields a conservative (upper-bound) uncertainty for σ. For the other terms independence remains a reasonable assumption.

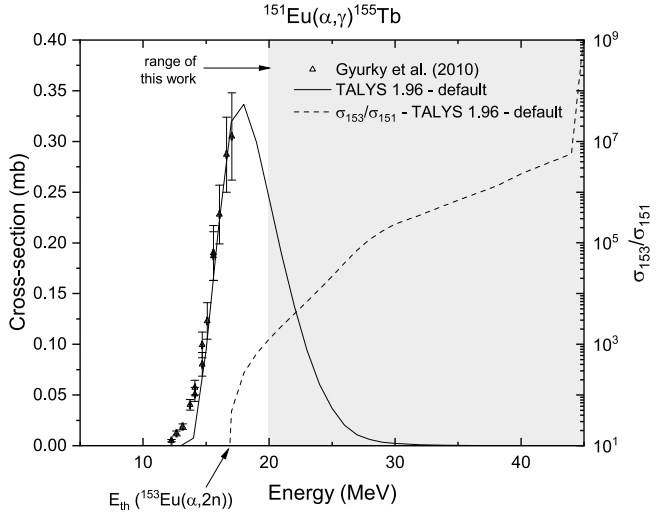

Figure 12. Influence of the ^{151}Eu(α, γ) process on ^{155}Tb production. Data from Gyürky *et al* [40] are compared with TALYS 1.96 simulations. The ratio $\sigma_{153}/\sigma_{151}$ (dashed line) indicates the relative contributions to ^{155}Tb production for the two europium isotopes obtained from TALYS 1.96 calculations. The gray area indicates the energy region of interest for this work.

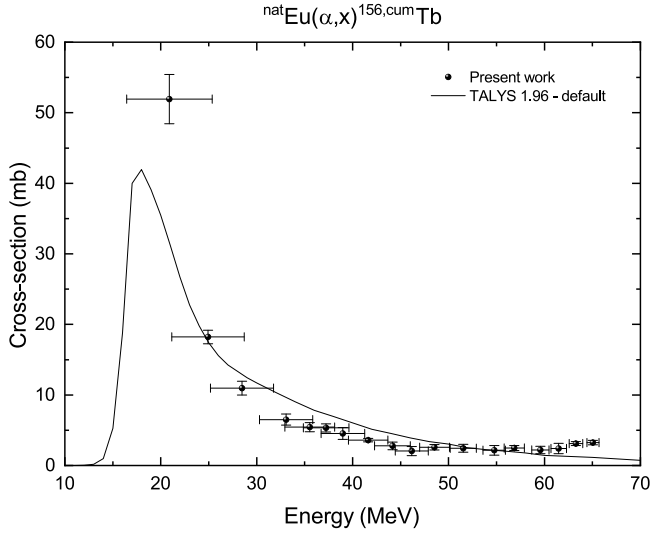

Figure 13. Cross-section for the ^{nat}Eu(α, x)$^{156g,\ cum}$Tb reaction. The cumulative results include contributions from two metastable states.

Repeated measurements of the same cross section contribute to lowering the overall uncertainty, with relative errors commonly falling within the range of 4% to 20%. However, higher uncertainties may arise when the independent production cross section of a radionuclide is inferred from cumulative measurements, particularly when contributions from parent radionuclides must be subtracted.

When the activity of a radionuclide is derived from repeated measurements or from multiple gamma peaks, the uncertainty of the weighted mean is estimated as the greater of

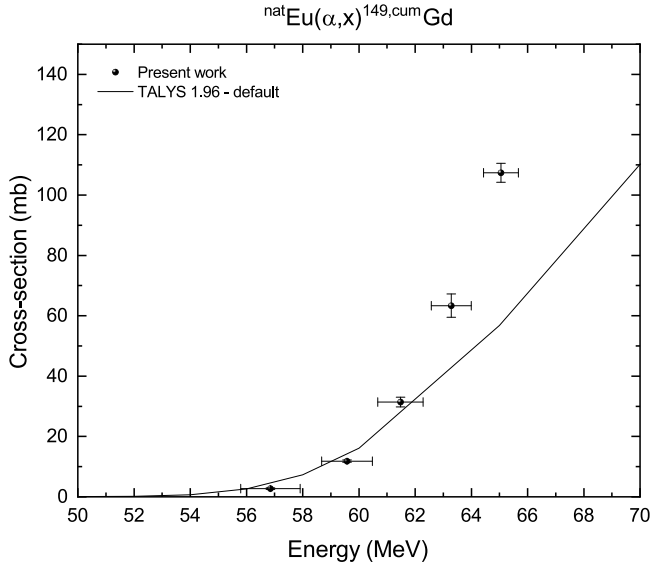

Figure 14. Cross-section for the ^{nat}Eu(α, x)$^{149,\ cum}$Gd reaction, including contributions from the decay of ^{149}Tb.

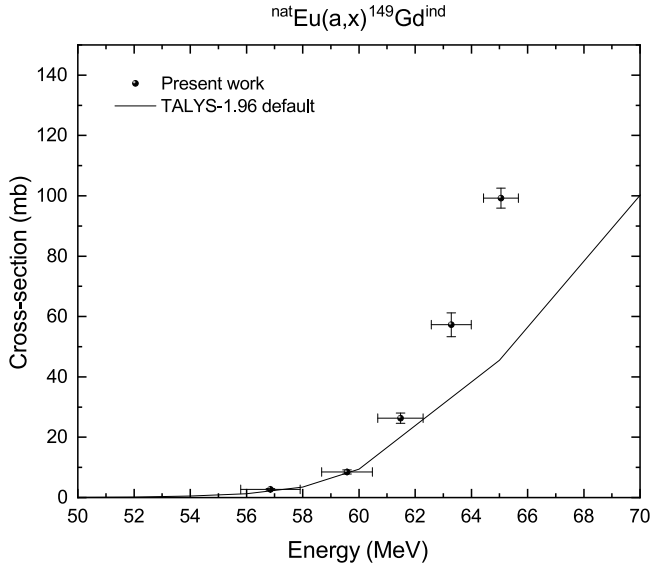

Figure 15. Cross-section for the ^{nat}Eu(α, x)^{149}Gd^{ind} reaction. The curve obtained with TALYS 1.96 nuclear code run with default options are compared with the experimental results.

the following two formulas:

$$\epsilon = \sqrt{\frac{1}{\sum_i \epsilon_i^{-2}}} \tag{4}$$

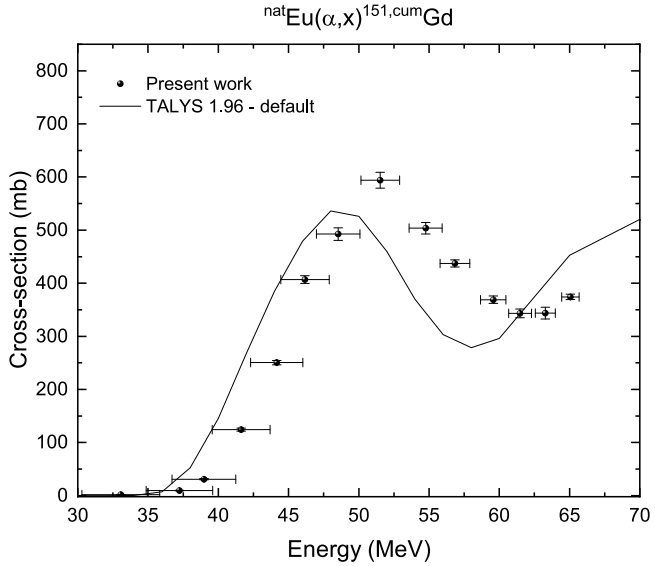

Figure 16. Cross-section for the ^{nat}Eu(α, x)$^{151,\ cum}$Gd reaction, including contributions from ^{151}Tb decay.

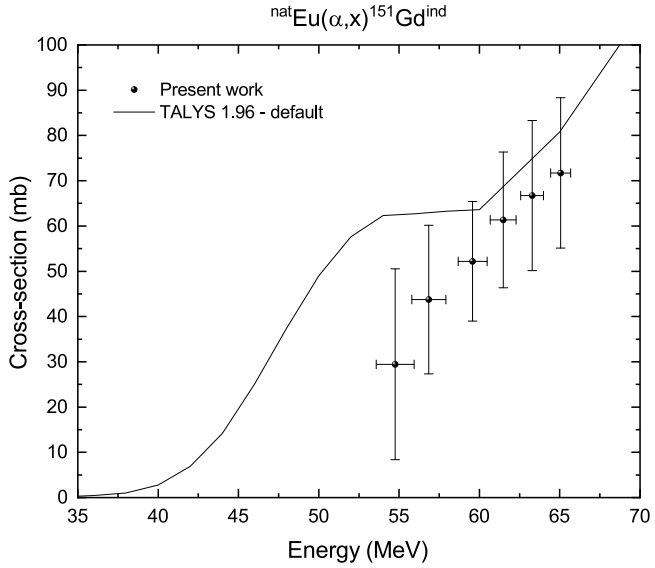

Figure 17. Cross-section for the ^{nat}Eu(α, x)^{151}Gd^{ind} reaction. The curve obtained with TALYS 1.96 nuclear code run with default options are compared with the experimental results.

and

$$\epsilon = \sqrt{\frac{\sum_i (x_i - \mu)^2 \cdot \epsilon_i^{-2}}{\sum_i \epsilon_i^{-2}}} \tag{5}$$

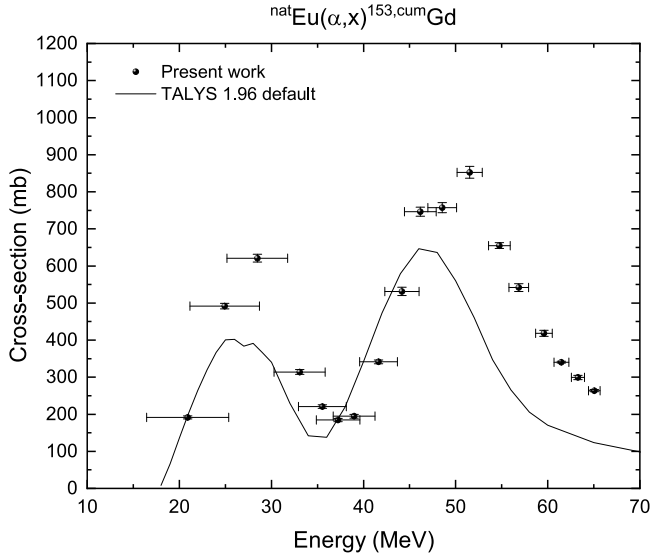

Figure 18. Cross-section for the ^{nat}Eu(α, x)$^{153,\ cum}$Gd reaction, including contributions from ^{153}Tb decay.

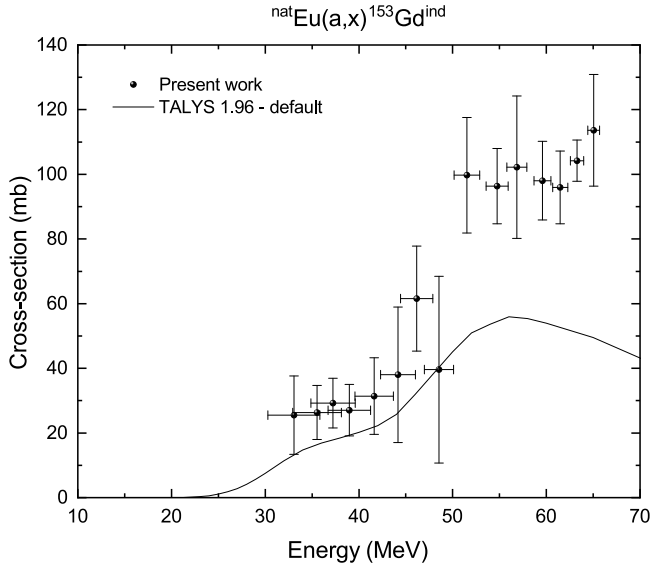

Figure 19. Cross-section for the ^{nat}Eu(α, x)^{153}Gd^{ind} reaction. The curve obtained with TALYS 1.96 nuclear code run with default options are compared with the experimental results.

where μ is the weighted mean, x_i denotes the ith measurement (or gamma peak), and ϵ_i is its associated standard uncertainty [34].

3.2. ^{nat}Eu(α, xn)^{149}Tb

The cross-section for the production of ^{149}Tb is shown in figure 3. TALYS 1.96 simulations overestimate the experimental values.

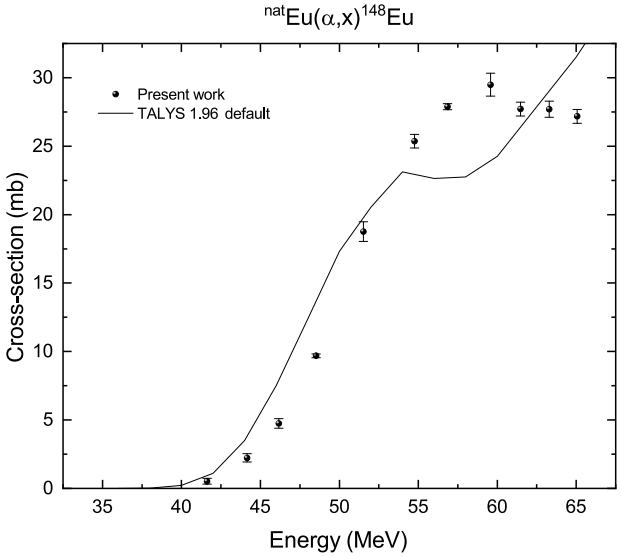

Figure 20. Cross-section for the ^{nat}Eu(α, x)^{148}Eu reaction. The curve obtained with TALYS 1.96 nuclear code run with default options are compared with the experimental results.

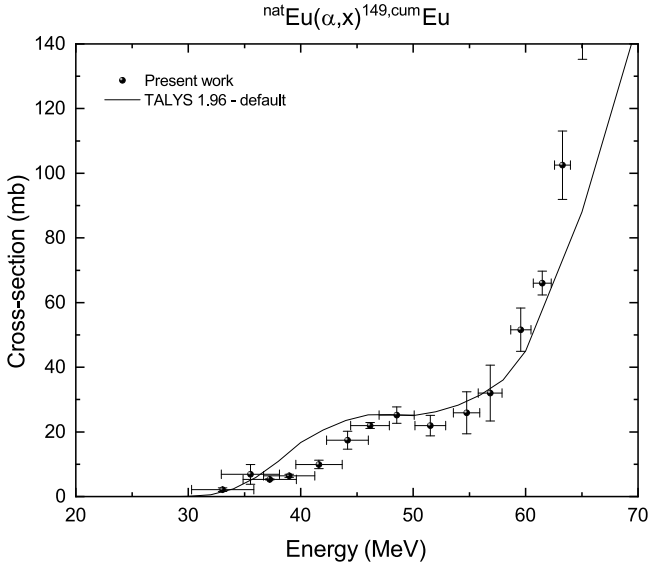

Figure 21. Cross-section for the ^{nat}Eu(α, x)$^{149,\ cum}$Eu reaction, including contributions from ^{149}Gd and ^{149}Tb decays.

The detection of ^{149}Tb is particularly challenging due to its low cross-sections, short half-life ($T_{1/2} = 4.118$ h), and the presence of gamma emissions in a high-noise energy region affected by Compton scattering. Consequently, data acquisition was limited to energies down to 59 MeV. In the presented energy range, the production of ^{149}Tb is entirely due to the ^{151}Eu(α, 6n) reaction ($E_{th} = 50.1$ MeV), as production from the ^{153}Eu isotope is not possible below the threshold energy of 65.2 MeV.

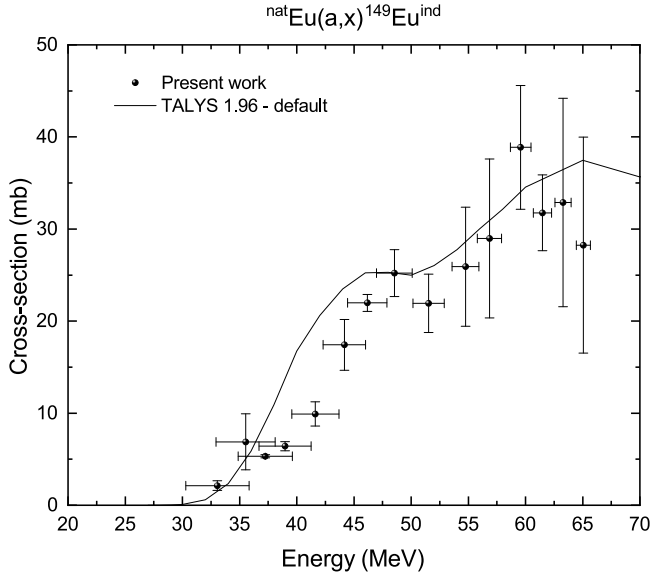

Figure 22. Cross-section for the ^{nat}Eu(α, x)^{149}Eu^{ind} reaction. The curve obtained with TALYS 1.96 nuclear code run with default options are compared with the experimental results.

3.3. ^{nat}Eu(α, xn)^{150}Tb

Figure 4 presents the cross-section for the ^{150}Tb production. Theoretical calculations using the TALYS 1.96 nuclear code with default settings failed to replicate the experimental data accurately.

3.4. ^{nat}Eu(α, xn)^{151}Tb

The measured cross-section for ^{151}Tb production is presented in figure 5, along with TALYS 1.96 simulation results. The code describes the overall cross-section shape and intensity well, but an energy shift of approximately 5 MeV is observed. The observed energy shift is clearly visible not only in this cross-section, but also consistently across all the following ones. This suggests that the shift is not an experimental artifact, especially since it is already present at high energies where the energy determination is largely reliable. The production route via ^{151}Eu(α, 4n) and ^{153}Eu(α, 6n), as listed in table 1, are discernible in the double-peak structure of the excitation function.

3.5. ^{nat}Eu(α, xn)^{152}Tb

The cross-section for the production of ^{152}Tb is illustrated in figure 6. TALYS 1.96 results follow the experimental trends but are shifted to lower energies. The reaction channels ^{151}Eu(α, 3n) and ^{153}Eu(α, 5n) contribute to the observed double-peak structure.

3.6. ^{nat}Eu(α, xn)^{153}Tb

The production cross-section of ^{153}Tb is presented in figure 7. Although TALYS 1.96 simulation reproduces the general shape of the cross-section, it underestimates the intensity of the peak and it is shifted to lower energies.

3.7. $^{nat}Eu(\alpha, xn)^{154}Tb$

The determination of the cross-sections for the production of the two metastable states of ^{154}Tb is complex due to the overlapping γ-ray emissions which originate from the same daughter nuclide ^{154}Gd. The γ-ray transitions used for analysis are provided in table 1. In particular, the peak at 540.18 keV is exclusively associated with the m1 state and was used to determine the production cross-section of ^{154m1}Tb. To determine the activity of the m2 state for each target, the counts of the 346.70 keV peak were corrected to account for the contribution from the m1 state to the same emission. This gamma line was chosen due to the relatively low intensity of the m1 contribution, which helps to minimize the error associated with the subtraction of counts. Moreover, the five point at higher energy have been corrected for the presence of ^{149}Gd emitting gamma rays at the same energy ($E_\gamma = 346.650$ keV, $I_\gamma = 23.7$ %).

TALYS 1.96 predictions agree reasonably well with the experimental data for the production of ^{154m2}Tb reported in figure 8.

Figure 9 shows the production cross-section for ^{154m1}Tb. TALYS 1.96 significantly underestimates the experimental data.

Determining the production cross-sections of the ground state of ^{154}Tb presents significant challenges. These include overlapping spectral peaks, substantial uncertainties in nuclear data (see table 1), and discrepancies in decay schemes and half-lives proposed by various authors, all of which hinder the establishment of a reliable dataset for this excitation function.

The branching ratios of the isomeric transition (IT) process for the metastable state were first measured by Lau *et al* [35]. According to their findings, the probability of the transition $m_2 \rightarrow m_1$ is 1.8%, while the Live Chart of Nuclides library reports that the m_2 isomer decays directly to the ground state [36]. For the transition $m_1 \rightarrow g$, Lau *et al* [35] determined a probability of 21.8%, whereas Bak *et al* [37] reported a lower value of 15%. Furthermore, the NUBASE2020 evaluation of nuclear physics properties [38] suggests a different ordering of the three isomers of ^{154}Tb, asserting that the available experimental data are insufficient to unambiguously identify the ground state. Additionally, the IT probability for these isomers is reported as either unknown or negligible.

In this study, our observations align with the hypothesis of a low or negligible contribution of ^{154m1}Tb (half-life: 9.4 h) to the growth of ^{154g}Tb (half-life: 21.5 h), consistent with results reported by Dellepiane *et al* [12]. In their investigation, the activity of ^{154g}Tb as a function of time exhibited a simple exponential decay curve, which is incompatible with the expected ground state activity growth due to an IT intensity of $I_{IT} = 21.8\%$ from ^{154m1}Tb. The absence of such growth strongly indicates that the contribution of ^{154m1}Tb to the ground state is negligible.

Due to limited measurements, typically only 3–5 data points within three days post-EOB, we were unable to fully track the decay. Nevertheless, when including contributions from metastable states, the derived activity values of ^{154g}Tb at EOB often exhibited time dependencies or values compatible with zero, suggesting that the observed ground state activity primarily originates from metastable state decay, which is unlikely. Conversely, when the contribution of ^{154m1}Tb was excluded, the $A^{EOB}(^{154g}Tb)$ values measured at different times post-EOB were mutually consistent.

This assumption, while strong, highlights the need for future studies to refine the gamma-transition intensities of ^{154}Tb, elucidate relationships between its isomeric states, and reconcile discrepancies in half-lives and branching ratios reported in the literature. These

efforts are essential to achieve a more accurate determination of the excitation function and production cross-sections of ^{154g}Tb.

Another source of uncertainty is the half-life of ^{154m1}Tb, initially accepted as 9.4 h 4 [2] but recently re-evaluated to 9.994 h 39 [39]. For this analysis, we used the former value. Additionally, uncertainties in gamma-emission intensities, which can reach up to 20%, further contribute to the overall uncertainty.

The production cross-section of ^{154g}Tb is shown in figure 10. TALYS 1.96 nuclear code overestimate of a factor 2 the experimental points.

3.8. ^{nat}Eu(α, xn)^{155}Tb

The cross-section for the production of ^{155}Tb is presented in figure 11. This reaction primarily proceeds via ^{153}Eu(α, 2n), while the ^{151}Eu(α, γ) contribution is negligible, as confirmed by simulations and the results from Gyürky *et al* [40] and from Moiseeva *et al* [22]. Figure 12 presents the experimental data from Gyürky *et al* (2010) [40], compared with TALYS 1.96 predictions and the theoretical contribution of ^{153}Eu relative to ^{151}Eu. This theoretical value was obtained by calculating the ratio between the production cross-sections of ^{155}Tb on ^{153}Eu and ^{151}Eu, based on TALYS 1.96 simulations. The use of this approach is supported by the good agreement observed between the theoretical predictions and the experimental data in both figures 11 and 12. The results suggest a minimal impact from ^{151}Eu in the studied energy range. This is supported by the fact that Moiseeva *et al* [22] which reported no production of ^{155}Tb through the reaction ^{151}Eu(α, γ) in the 19–60 MeV energy range.

3.9. ^{nat}Eu(α, xn)^{156g}Tb

^{156}Tb has two metastable states in addition to its ground state. However, determining the production cross-sections of ^{156m1}Tb ($T_{1/2} = 24.4$ h) and ^{156m2}Tb ($T_{1/2} = 5.3$ h) was not feasible. The primary challenge for ^{156m1}Tb is that its characteristic gamma emission at 49.630 keV overlaps with the x-ray emissions of Tb, Gd, and Eu. For ^{156m2}Tb, the only reported gamma emission at 88.4 keV has an intensity of less than 1.15% [2], though a precise value is not available in the literature.

The cumulative cross-section for ^{156g}Tb, which includes contributions from metastable states, was determined by starting the measurements of the activity of ^{156g}Tb 8 d after the irradiation and it is presented in figure 13. TALYS 1.96 predictions show good agreement with the experimental data, although the code underestimates the cross-section at the energy of 21 MeV.

3.10. ^{nat}Eu(α, x)^{149}Gd

The cumulative production of ^{149}Gd, including the decay contribution of ^{149}Tb, is shown in figure 14. Measurements were taken one week post-irradiation to ensure complete decay of the parent nuclide, also minimizing background noise. TALYS 1.96 predictions underestimate the experimental results.

The independent cross-section of production of ^{149}Gd in shown in figure 15. Also in this case the simulations underestimate the data.

3.11. $^{nat}Eu(\alpha, x)^{151}Gd$

The production of ^{151}Gd is primarily due to the decay of ^{151}Tb, as confirmed by comparing figure 16 and figure 5. The cross-section values were measured 1–4 months post-irradiation, ensuring accurate cumulative measurements.

The independent cross-section of production of ^{151}Gd in shown in figure 17 where it is compared to the TALYS 1.96 simulation curve that slightly overestimate our results. It was possible to determine the independent cross-section only down to 55 MeV since for lower energies the uncertainties were too high with respect to the value.

3.12. $^{nat}Eu(\alpha, x)^{153}Gd$

The cumulative production cross-section for ^{153}Gd, including the decay contribution of ^{153}Tb, is shown in figure 18. Measurements were taken more than 1 month post-irradiation, ensuring accurate data.

The independent cross-section of production of ^{153}Gd in shown in figure 19 where it is compared to the TALYS 1.96 simulation curve that underestimates our results but shows a similar trend. It was possible to determine the independent cross-section only down to 32 MeV. The excitation function shows a scattered behavior around 50 MeV and high uncertainties coming from the error propagation rule.

3.13. $^{nat}Eu(\alpha, x)^{148}Eu$

The cross-section for the ^{148}Eu production is shown in figure 20. TALYS 1.96 presents the energy shift common also to all the previous data, and underestimate the shoulder region between 55–60 MeV.

3.14. $^{nat}Eu(\alpha, x)^{149}Eu$

The cumulative cross-section for ^{149}Eu, originating from the decay chain $^{149}\text{Tb} \rightarrow {}^{149}\text{Gd} \rightarrow {}^{149}\text{Eu}$, is presented in figure 21. The predictions of TALYS 1.96 match well with the experimental results.

The independent cross-section of production of ^{149}Eu in shown in figure 22 where it is compared to the TALYS 1.96 simulation is in agreement with the experimental data.

4. Production of ^{155}Tb from highly enriched ^{153}Eu targets

The production of ^{155}Tb is of significant interest due to its potential applications in nuclear medicine, particularly in theranostic approaches where it can be used alongside other terbium isotopes for imaging and therapy. While various production methods exist, the direct route via the $^{153}\text{Eu}(\alpha, 2n)$ reaction offers a potential advantage in terms of simplicity and the possibility of obtaining ^{155}Tb in a NCA form. However, optimizing this production pathway requires careful assessment of yield, radionuclidic purity, and feasibility under practical irradiation conditions.

The end-of-bombardment (EOB) thick target yield, TTY^{EOB} (in $\text{MBq}\,\mu\text{A}^{-1}$), which quantifies the activity produced per unit of beam current, depends on irradiation time in a nonlinear fashion. It is related to the physical yield via the following equation [41]:

$$\mathrm{TTY}^{\mathrm{EOB}}(E;\,\Delta E;\,t_{\mathrm{irr}}) = \frac{1-\mathrm{e}^{-\lambda t_{irr}}}{\lambda}\cdot\alpha_{\mathrm{phys}}(E,\,\Delta E) = \frac{N_{\mathrm{A}}\cdot(1-\mathrm{e}^{-\lambda t_{\mathrm{irr}}})}{M\cdot Ze}\int_{E-\Delta E}^{E}\frac{\sigma(E')}{\left(\frac{1}{\rho}\frac{\mathrm{d}E}{\mathrm{d}x}(E')\right)}\,\mathrm{d}E' \tag{6}$$

In this equation, α_{phys} (in MBq C^{-1}) is the physical thick target yield [41], E is the incident energy of the alpha particles, ΔE is the energy dissipated in the target material, and $\frac{1}{\rho}\frac{\mathrm{d}E}{\mathrm{d}x}$ represents the mass stopping power. The constants N_{A}, M, λ, Z, and e correspond respectively to Avogadro's number, molar mass, decay constant, atomic number of the incident particle, and the elementary charge, as previously defined in equation (1).

To evaluate the viability of the approach presented in this work, we estimated the yield and purity of ^{155}Tb assuming an ideal 100% enriched ^{153}Eu target. The following hypotheses were considered to establish a simplified model for the reaction dynamics and to assess the impact of potential contaminants:

1. *Production of ^{155}Tb*. It is assumed that ^{155}Tb is exclusively produced via the ^{153}Eu(α, 2*n*) reaction within the studied energy range. This assumption is corroborated by TALYS 1.96 nuclear reaction modeling, which accurately reproduces the ^{151}Eu(α, γ) cross-section data from Gyürky *et al* [40]. Contributions to ^{155}Tb production at energies above 20 MeV are considered negligible.
2. *Production of ^{154}Tb Isomers*. All ^{154}Tb isomers produced above the threshold energy for the ^{153}Eu(α, 3*n*) reaction (25.5 MeV) are attributed solely to this process, neglecting contributions from ^{151}Eu(α, *n*). This assumption is both conservative and reasonable. Experimental data and simulations (figures 8, 9, 10) indicate that, above 25 MeV, only a diminishing tail remains of the ^{154}Tb production curve associated with ^{151}Eu. If a fraction of ^{154}Tb is indeed produced via ^{151}Eu, its exclusion from the ^{153}Eu target would increase the purity of ^{155}Tb, as ^{154}Tb acts as a contaminant.
3. *Exclusion of ^{153}Tb*. Since no reliable assumptions can be made for the production of ^{153}Tb on enriched ^{153}Eu, the analysis is restricted to energies below the threshold of the ^{153}Eu(α, 4*n*) reaction (32.5 MeV), where ^{153}Tb production is energetically impossible.

The irradiation time has been chosen to be 10 h to perform a comparison with the data from [24]. However a longer time may be advantageous both in terms of yield and purity since the production of ^{154}Tb isomers reach the saturation value in a shorter time, increasing the ratio between ^{155}Tb and ^{154x}Tb activities.

The activity per unit of current at EOB of ^{155}Tb produced in these conditions is reported in figure 23. The yield obtained in this study is 10%–20% lower compared to the values reported by Kormazeva *et al* [24] over the entire investigated range. This slightly lower yields can be ascribed to the denser energy sampling around the ^{155}Tb excitation-function maximum in that work. In our case, a finer energy grid was not feasible because α-particle straggling would have introduced large uncertainties in the effective beam energy. At overlapping energies, the cross sections remain consistent within uncertainties after rescaling for the isotopic enrichment with data of Kormazeva *et al* [24].

4.1. Optimization methodology

In this study, we employed the Non-dominated Sorting Genetic algorithm II (NSGA-II) to optimize the production parameters for ^{155}Tb. NSGA-II is a widely recognized multi-objective evolutionary algorithm renowned for its efficiency in handling complex

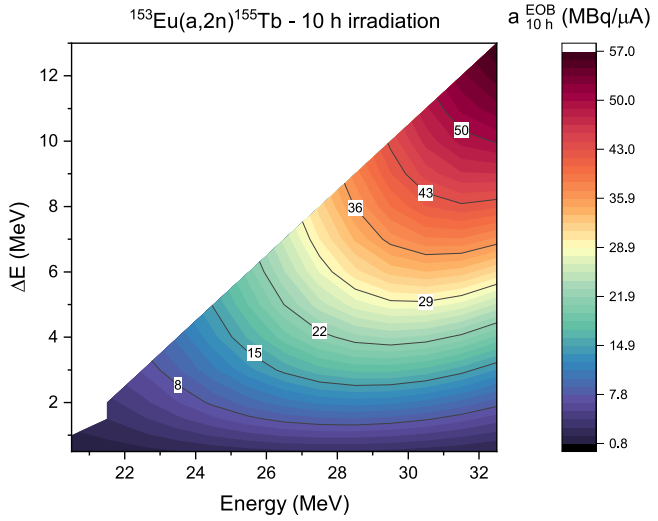

Figure 23. Activity per unit of current of ^{155}Tb at the EOB, as function of the incident alpha beam energy and of the loss of energy within the target. A 10 h long irradiation has been assumed. The black contour lines correspond to iso-yield curves, with the labels indicating the activity per unit current at EOB along each contour.

optimization problems involving conflicting objectives [42]. The algorithm operates by iteratively evolving a population of potential solutions through selection, crossover, and mutation, guided by non-dominated sorting and crowding distance mechanisms to ensure convergence towards a diverse Pareto-optimal front.

The optimization process was structured as follows:

1. *Decision Variables*. The key parameters influencing ^{155}Tb production—beam energy E, target thickness S, and post-EOB cooling time t—were selected as decision variables. Their ranges were set according to the activity grid used for interpolation: $E \in [20.5, 32.5]$ MeV, S corresponding to an energy loss $\Delta E \in [0.5 - 13]$ MeV, and $t \in [0, 864000]$ s (0–10 d).
2. *Objective Functions*.
   - *Yield maximization*: $Y(E, S, t) = A_{155}(t)$, i.e. the activity of ^{155}Tb after cooling time t, obtained from interpolation of the thick-target yield grid and propagated in time using the decay equations.
   - *Purity maximization*: $P(E, S, t) = A_{155}(t)/\sum_i A_i(t)$, where the denominator includes all isotopic contaminants. P was clipped to the interval [0, 1] to avoid spurious values.

To fit the NSGA-II minimization framework, the fitness vector was defined as

$$F(E, S, t) = (-Y(E, S, t), \ -P(E, S, t)),$$

with equal weighting of the two objectives. No normalization was applied, since NSGA-II handles differently scaled objectives via Pareto dominance.

3. *Algorithm Configuration*. The NSGA-II parameters were set to ensure convergence while maintaining computational efficiency. Specifically, we employed a population size of 100, 200 generations per run, simulated binary crossover with probability 0.9 and distribution index $\eta_c = 15$, and polynomial mutation with probability 0.2 and distribution index $\eta_m = 20$. The algorithm was implemented using the `pymoo` optimization library in Python [43]. Two constraints were enforced: (i) $E - S > 19$ MeV

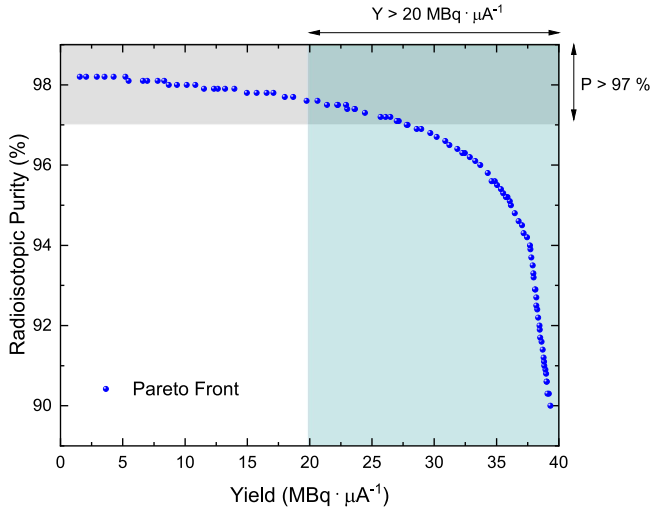

Figure 24. Pareto front obtained from the optimization process. Each point represents a trade-off between ^{155}Tb yield and radioisotopic purity. The gray region represent region where Radioisotopic Purity is higher than 97 %, while the green region cover the points where yield is higher than 20 MBq μA^{-1}.

to ensure validity of the interpolation domain, and (ii) $P \geqslant 0.90$ to guarantee minimum purity. With this configuration, results from 30 independent runs with distinct random seeds produced overlapping Pareto fronts, demonstrating the absence of seed dependence and confirming the algorithmic robustness of the optimization procedure (see section 4.3).

By applying NSGA-II, we effectively navigated the trade-offs between yield and purity in ^{155}Tb production, identifying a set of Pareto-optimal solutions that offer a spectrum of choices depending on specific application requirements. This methodology underscores the utility of advanced multi-objective optimization techniques in radionuclide production processes.

4.2. Optimization results

The optimization process yielded a Pareto front that illustrates the trade-off between the two competing objectives: maximizing the yield of ^{155}Tb and enhancing its radionuclidic purity. The Pareto front, shown in figure 24, provides a set of non-dominated solutions where any improvement in one objective results in a compromise in the other.

This visual representation facilitates the selection of production parameters based on specific application requirements, balancing yield and purity as needed.

The obtained points have been filtered by considering the following constrains: Yield higher than 20 MBq μA^{-1}, Radioisotopic Purity greater than 97% and a decay time longer than 2 h to ensure the time needed for the target manipulation. These constrains lead to an energy of the beam of 28.5 MeV and a loss of energy of 5 MeV that corresponds to a mass thickness of 44.6 mg cm^{-2} of Eu metal form, i.e. 85 μm of Eu considering the nominal density of 5.244 g cm^{-3} with a yield of 27 MBq μA^{-1}. If we consider an oxide target, a mass thickness of 40.0 mg cm^{-2} are required to degrade the energy from 28.5 MeV to 23.5 MeV, equivalent to 54 μm of europium oxide assuming the density of 7.4 g cm^{-3}. In this case the

Yield is reduced to approximately 21 MBq μA^{-1} considering the difference in thickness and the factor $m_{Eu\%} = 0.86\%$ obtained as ratio between two times the molar mass of Eu and the molar mass of Eu_2O_3. The Radioisotopic Purity obtained in both conditions is of 97% at the EOB that remains constant during the time given the negligible contribute of the ^{154}Tb isomers and the comparable half-life of ^{156g}Tb that represents the main contaminant at all cooling time. In practical scenarios, where enrichment levels of ^{153}Eu reach 99.8% as reported by Kormazeva *et al* [24], the eventual presence of ^{151}Eu in the target may affect the radioisotopic purity: it would lead to the co-production of ^{153}Tb that is not possible to remove chemically or by decay considering its half-life of 2.34 d. Nevertheless, experimental results on realistic targets indicate that the fraction of ^{153}Tb remains below 0.1% in this range [24], so the overall impact on radioisotopic purity is minor. There is accordance between the results presented here and the one obtained by Kormazeva *et al* (2024), that determined a percentage of ^{156}Tb between 3% and 5% when irradiating enriched ^{153}Eu in this energy range [24].

The energy required for the alpha beam is similar to the one that is commonly used to produce the therapeutic relevant radionuclide ^{211}At [44].

In table 6, the results of this work are compared with other direct production routes of ^{155}Tb. While some of the proposed routes yield higher production rates, none of the direct nuclear reactions achieves a radionuclidic purity as high as 97 %. It should be noted, however, that in this work a target composed of 100 % enriched ^{153}Eu was assumed, whereas other studies based on ^{155}Gd or ^{156}Gd used the highest enrichment levels currently available. Nevertheless, [24] succeeded in obtaining ^{153}Eu-enriched targets up to 99.8 %, a value very close to the one assumed in this study. On the other hand, enriching targets in ^{155}Gd or ^{156}Gd is more challenging due to their low natural isotopic abundances, maximum enrichment obtained currently are 91.9 % for ^{155}Gd and 93.3 % for ^{156}Gd [12]. In presence of ^{156}Gd, ^{156}Tb will always be produced [13]. It has been demonstrated that, in the case of the ^{155}Gd(p, n)^{155}Tb reaction, ^{155}Tb can be produced with a quality suitable for medical applications using low-energy proton beams and ^{155}Gd-enriched targets, provided that the ^{156}Gd impurity content does not exceed 2%. Under these conditions, the increase in patient dose due to contaminant radioisotopes remains below the 10 % threshold [18]. The production of ^{155}Tb through the ^{155}Gd(d, $2n$) reaction has also been investigated, as reported by Wang *et al* [15]. In this case, long decay times of about 14 d (about 3 half-lives of ^{155}Tb) are required to reach a radionuclidic purity of 89%, which however comes at the cost of reduced yield.

Compared to the indirect route ^{159}Tb(p, $5n$)^{155}Dy $\rightarrow$ ^{155}Tb [31], which provides both higher yield and purity but requires very thick targets and two separation steps, the direct α-induced route on enriched ^{153}Eu is less productive but technically simpler and uniquely allows the production of no-carrier-added (NCA) ^{155}Tb, an important advantage for medical applications. Simple strategies of chemical separation of Tb from Eu target have already been discussed in the literature [45], and are not addressed in detail here. These factors support the consideration of this route as a promising alternative for ^{155}Tb production.

The results should be verified experimentally by performing irradiation runs of thick targets of enriched ^{153}Eu. Alpha particles in the considered energy range have a high LET, which typically limits the maximum beam current that can be safely applied to the target due to thermal constraints. A detailed thermal analysis was not attempted in this work, since the target stability depends not only on the matrix material (Eu_2O_3) but also on the specific preparation technique and the cooling design adopted by each facility. As such, meaningful simulations (e.g. ANSYS-based) can only be performed once the actual target configuration is defined. We therefore limited our discussion to underlining the importance of thermal

Table 6. Comparison of different various production methods for ^{155}Tb. Only the α^{EOB}_{phys} has been reported to be compared with the results from other works. The decay time to reach the maximum purity has been reported (t_d). [(a)] In the case of the indirect process, the activity per unit of current in an irradiation scenario of 30 h and a waiting time between the two required separation procedure of 40 h is reported, since a definition of physical yield for the indirect process is not possible.

Process	Source	Energy (MeV)	Target form	Target thickness (μm)	α^{EOB}_{phys} (MBq μA^{-1} h^{-1})	t_d	RNP
^{155}Gd(p, n)	[12]	10.5	(^{155}Gd)Gd_2O_3	300	3.4	4 d	93%
^{156}Gd(p, 2n)	[12]	18.5	(^{156}Gd)Gd_2O_3	300	14.3	4 d	89%
^{155}Gd(d, 2n)	[15]	15.1	(^{155}Gd)Gd_2O_3	390	10.2	14 d	89%
^{153}Eu(α, 2n)	this work	28.5	metal ^{153}Eu	85	2.8	/	97%
^{153}Eu(α, 2n)	this work	28.5	(^{153}Eu)Eu_2O_3	54	2.2	/	97%
^{159}Tb(p, 5n)^{155}Dy $\rightarrow ^{155}$Tb	[31]	59	Tb_2O_3	3000	1200 MBq μA^{-1} [(a)]	/	>99.9%

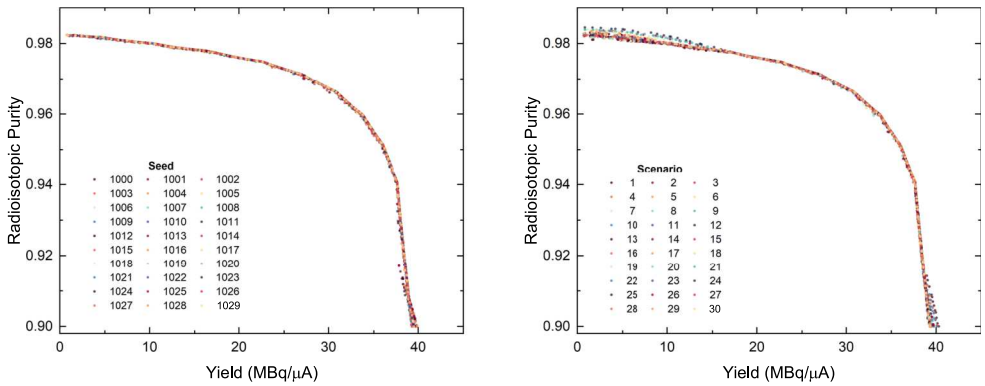

Figure 25. Comparison of Pareto fronts under two robustness analyses. (a) Algorithmic robustness: Pareto fronts from 30 runs with distinct random seeds (λ fixed). Fronts obtained with different random seeds are essentially overlapping, indicating absence of seed dependence. (b) Physical sensitivity: Pareto fronts from 30 Monte Carlo scenarios with perturbed decay constants ($\pm 5\%$).

constraints, and we note that future investigations on target engineering and cooling strategies will be essential to complement the present nuclear data.

4.3. Robustness and sensitivity analysis

We assessed two distinct sources of variability affecting the Pareto front in the (Yield, Purity) objective space:

1. *Algorithmic robustness*. variance induced by the evolutionary optimizer. In this case, all decay constants were fixed to their nominal values, and 30 independent NSGA-II optimizations were performed with different seeds (1000–1029).
2. *Physical sensitivity*. propagation of experimental uncertainty in the nuclear decay data. Here, the decay constants $\{\lambda_i\}$ were perturbed with multiplicative Gaussian noise (log-normal approximation) with relative standard deviation $\sigma_{\mathrm{rel}} = 5\%$. For each scenario, the optimizer seed was held fixed in order to isolate the effect of λ perturbations.

Figure 25(a) illustrates the dispersion of Pareto fronts obtained with 30 distinct seeds. The following behaviors have been observed:

1. Across seeds, Pareto fronts remain tightly clustered around the nominal front. Occasional outliers can be observed, corresponding to under-converged runs, which typically vanish when the evolutionary budget (population size and/or number of generations) is increased.
2. No systematic bifurcations of the front were observed once convergence was ensured, confirming that the optimization procedure is robust to stochastic variation.

Under $\pm 5\%$ perturbations of the decay constants, the Pareto fronts remain tightly grouped around the nominal curve (figure 25(b)). The deformation is not a uniform shift but rather a tilt of the front: purity is marginally improved at the low-yield/high-purity end, while yield is slightly increased at the low-purity/high-yield end. The Pareto knee remains essentially preserved.

5. Conclusion

This study represents the first comprehensive investigation into the nuclear cross-sections of ^{nat}Eu(α, x) reactions, focusing on the production of medically relevant terbium isotopes over an energy range of 20–65 MeV. By employing europium oxide nanopowder targets and advanced gamma spectrometry techniques, we have successfully determined excitation functions for various terbium isotopes and non isotopic contaminants. The consistent $\sim$5 MeV energy shift observed between TALYS calculations and the measured excitation functions highlights the need for future theoretical work focused on refining level-density models and α-optical potentials, in order to achieve improved predictive accuracy.

The consideration that ^{155}Tb production can be attributed mainly to the ^{153}Eu(α, 2n) reaction paved the way for optimizing production routes using enriched ^{153}Eu targets. Multi-objective optimization using NSGA-II demonstrated that high yields and radionuclidic purity (97%) of ^{155}Tb are achievable under beam energy and energy loss within the target conditions of 28.5 and 5 MeV respectively. These results underscore the potential of alpha-particle irradiation as a viable method for producing high-purity ^{155}Tb. Importantly, robustness and sensitivity analyses confirmed that the optimization outcomes are stable with respect to both algorithmic stochasticity and $\pm$5% uncertainties in decay data, further strengthening the reliability of the proposed optimization method.

Comparison with other direct production routes, including proton and deuteron-induced reactions on gadolinium targets, reveals that the proposed method offers competitive yields and superior radionuclidic purity, considering the present enrichment possibilities of targets of ^{155}Gd, without requiring extended decay times.

Future work should focus on scaling up the production using enriched europium targets and conducting irradiation studies with optimized parameters to validate the predicted yields and purities. As alpha particles impose stricter thermal constraints, preliminary thermal characterization of Eu_2O_3 targets a function of temperature and density is recommended to ensure safe and efficient irradiation conditions. Additionally, further investigations into the decay schemes and isomeric states of ^{154}Tb that represents a key source of uncertainty in the theoretical determination of the purity of the final product. These efforts will contribute to establishing reliable production methods for terbium isotopes, thereby accelerating their integration into clinical settings for diagnostic and therapeutic purposes.

Acknowledgments

Inquiries regarding this work may be directed to Dr. Simone Manenti at simone.manenti@unimi.it.

Data availability statement

All data that support the findings of this study are included within the article (and any supplementary files).

Funding

This work has been funded by the CSN5 of the Italian National Institute of Nuclear Physics (INFN) through the project REMIX and by the CSN3 of INFN through the project

SPES_MED. The mobility has been partially supported by the ENEN2plus project (HORIZON-EURATOM-2021-NRT-01-13 101061677) funded by the European Union. The cyclotron Arronax is supported by CNRS, Inserm, INCa, the Nantes University, the Regional Council of Pays de la Loire, local authorities, the French government and the European Union. This work has been supported in part by the French National Research Agency (ANR) 'France 2030 investment plan' under the references I-SITE NExT (ANR-16-IDEX-0007), and Labex DHOLMEN, by financial support from the Pays de la Loire Region and by a Grant from INCa-DGOS-INSERM-ITMO Cancer_18011 (SIRIC ILIAD).

Author contributions

Michele Colucci 0000-0001-7202-7710
Conceptualization (equal), Data curation (lead), Formal analysis (lead), Investigation (lead), Methodology (lead), Supervision (equal), Validation (equal), Visualization (lead), Writing – original draft (lead), Writing – review & editing (equal)

Etienne Nigron 0000-0002-8265-8337
Investigation (equal), Validation (equal), Visualization (equal), Writing – review & editing (equal)

Ferid Haddad 0000-0001-6971-5969
Funding acquisition (equal), Investigation (equal), Project administration (equal), Resources (equal), Supervision (equal), Validation (equal), Visualization (equal), Writing – review & editing (equal)

Arnaud Guertin 0000-0002-9077-0994
Investigation (equal), Supervision (equal), Validation (equal), Visualization (equal), Writing – review & editing (equal)

Eugenio Gibertini 0000-0002-2610-5500
Investigation (equal), Writing – review & editing (supporting)

Luca Magagnin 0000-0001-5553-6441
Investigation (equal), Writing – review & editing (supporting)

Flavia Maria Groppi Garlandini 0000-0002-8987-8375
Conceptualization (equal), Funding acquisition (equal), Investigation (equal), Methodology (equal), Project administration (equal), Resources (equal), Supervision (equal), Validation (equal), Visualization (equal), Writing – review & editing (equal)

Simone Manenti 0000-0003-4106-058X
Conceptualization (equal), Funding acquisition (equal), Investigation (equal), Project administration (equal), Resources (equal), Supervision (equal), Validation (equal), Visualization (equal), Writing – review & editing (equal)

References

[1] Müller C, Domnanich K A, Umbricht C A and van der Meulen N P 2018 Scandium and terbium radionuclides for radiotheranostics: current state of development towards clinical application *Br. J. Radiol.* **91** 20180074

[2] National Nuclear Data Center, Brookhaven National Laboratory, NuDat 3.0 (Nuclear Structure and Decay Data), accessed: 2024-12-16, https://www.nndc.bnl.gov/nudat3/

[3] Müller C, Vermeulen C, Köster U, Johnston K, Türler A, Schibli R and van der Meulen N P 2016 Alpha-PET with terbium-149: evidence and perspectives for radiotheragnostics *EJNMMI Radiopharm. Chem.* **1** 5

[4] Müller C *et al* 2019 Preclinical investigations and first-in-human application of ^{152}Tb-PSMA-617 for PET/CT imaging of prostate cancer *EJNMMI Res.* **9** 68

[5] Baum R P *et al* 2017 Clinical evaluation of the radiolanthanide terbium-152: first-in-human PET/CT with ^{152}Tb-DOTATOC *Dalton Trans.* **46** 14638–46

[6] Müller C *et al* 2014 Future prospects for SPECT imaging using the radiolanthanide terbium-155 - production and preclinical evaluation in tumor-bearing mice *Nucl. Med. Biol.* **41** e58–e65

[7] Buchegger F, Perillo-Adamer F, Dupertuis Y M and Delaloye A B 2006 Auger radiation targeted into DNA: a therapy perspective *Eur. J. Nucl. Med. Mol. Imaging* **33** 1352–63

[8] Baum R P *et al* 2021 First-in-human application of terbium-161: A feasibility study using ^{161}Tb-DOTATOC *J. Nucl. Med.* **62** 1391-–1397

[9] Ichinkhorloo D, Aikawa M, Tsoodol Z, Komori Y and Haba H 2023 Production cross sections of terbium and gadolinium radioisotopes from the deuteron-induced reactions on natural gadolinium up to 24 MeV *Nucl. Instrum. Methods Phys. Res., Sect. B* **536** 30–7

[10] Szelecsényi F, Kovács Z, Nagatsu K, Zhang M R and Suzuki K 2016 Investigation of deuteron-induced reactions on ^{nat}Gd up to 30 MeV: possibility of production of medically relevant ^{155}Tb and ^{161}Tb radioisotopes *J. Radioanal. Nucl. Chem.* **307** 1877–1881

[11] Moiseeva A N, Aliev R A, Furkina E B, Novikov V I and Unezhev V N 2022 New method for production of ^{155}Tb via ^{155}Dy by irradiation of ^{nat}Gd by medium energy alpha particles *Nucl. Med. Biol.* **106-107** 5261

[12] Dellepiane G, Casolaro P, Favaretto C, Grundler P V, Mateu I, Scampoli P, Talip Z, van der Meulen N P and Braccini S 2022 Cross section measurement of terbium radioisotopes for an optimized ^{155}Tb production with an 18 MeV medical PET cyclotron *Appl. Radiat. Isot.* **184** 110175

[13] Colombi A and Fontana A 2024 Comparative study of 155Tb production via 155Dy precursor with p, d and α beams on natural targets for medical applications *Appl. Radiat. Isot.* **212** 111443

[14] Güray R T, Özkan N, Yalç ın C, Rauscher T, Gyürky G, Farkas J, Fülöp Z, Halász Z and Somorjai E 2015 Measurements of ^{152}Gd(p, γ)^{153}Tb and ^{152}Gd(p, n)^{152}Tb reaction cross sections for the astrophysical γ process *Phys. Rev. C* **91** 055809

[15] Wang Y, Sounalet T, Guertin A, Nigron E, Michel N and Haddad F 2023 Study of terbium production from enriched Gd targets via the reaction 155Gd(d,2n)155Tb *Appl. Radiat. Isot.* **201** 110996

[16] Favaretto C *et al* 2021 Cyclotron production and radiochemical purification of terbium-155 for SPECT imaging *EJNMMI Radiopharm. Chem.* **6** 1–17

[17] Dmitriev P, Molin G and Dmitrieva Z 1989 Production of 155 Tb for nuclear medicine by reactions 155 Gd (p, n), 156 Gd (p, 2n), 155 Gd (d2n) *At. Energ.* **66** 419–21

[18] Barbaro F, Canton L, Uzunov N, Nardo L D and Melendez-Alafort L 2024 ^{155}Tb production by cyclotrons: what level of ^{155}gd enrichment allows clinical applications? *EJNMMI Phys.* **11** 26

[19] Nigron E, Guertin A, Haddad F, Granger L, Rayer M and Rintaud A 2023 Can we reach suitable 161Tb purity for medical applications using the 160Gd(d, n) reaction? *Appl. Radiat. Isot.* **200** 110927

[20] Tárkányi F, Ditrói F, Takács S, Csikai J, Hermanne A and Ignatyuk A V 2014 Activation cross-sections of long lived products of deuteron induced nuclear reactions on dysprosium up to 50 MeV *Appl. Radiat. Isot.* **83** 18–24

[21] Colucci M, Carminati S, Haddad F, Nigron E, Groppi F and Manenti S 2022 Excitation functions of deuteron induced nuclear reactions on dysprosium targets for the production of the theranostic relevant isotopes of terbium *Eur. Phys. J. Plus* **137** 1180

[22] Moiseeva A, Aliev R, Unezhev V, Gustova N, Madumarov A, Aksenov N and Zagryadskiy V 2021 Alpha particle induced reactions on ^{151}Eu: possibility of production of ^{152}Tb radioisotope for PET imaging *Nucl. Instrum. Methods Phys. Res., Sect. B* **497** 59–64
[23] Moiseeva A, Aliev R, Unezhev V, Zagryadskiy V, Latushkin S, Aksenov N, Gustova N, Voronuk M, Starodub G Y and Ogloblin A 2020 Cross section measurements of ^{151}Eu (3He, 5*n*) reaction: new opportunities for medical alpha emitter ^{149}Tb production *Sci. Rep.* **10** 508
[24] Kormazeva E, Ilyuschenko A, Novikov V, Moiseeva A, Khomenko I, Shpuntov D, Aksenov N, Voronuk M and Aliev R 2025 Alpha particle induced reactions on ^{153}Eu as possible routes for ^{152}Tb and ^{155}Tb production *Radiat. Phys. Chem.* **234** 112809
[25] Naskar N and Lahiri S 2021 Theranostic terbium radioisotopes: challenges in production for clinical application *Front. Med.* **8** 5
[26] Qaim S M, Scholten B and Neumaier B 2018 New developments in the production of theranostic pairs of radionuclides *J. Radioanal. Nucl. Chem.* **318** 1493–509
[27] Moiseeva A N, Favaretto C, Talip Z, Grundler P V and van der Meulen N P 2024 terbium sisters: current development status and upscaling opportunities *Front. Nucl. Med.* **4** 1472500
[28] Haddad F, Ferrer L, Guertin A, Carlier T, Michel N, Barbet J and Chatal J F 2008 ARRONAX, a high-energy and high-intensity cyclotron for nuclear medicine *Eur. J. Nucl. Med. Mol. Imaging* **35** 1377–87
[29] Ziegler J F, Ziegler M D and Biersack J P 2010 SRIM—The stopping and range of ions in matter (2010) *Nucl. Instrum. Methods Phys. Res., Sect. B* **268** 1818–23
[30] Hermanne A *et al* 2018 Reference cross sections for charged-particle monitor reactions *Nucl. Data Sheets* **148** 338–82
[31] Colucci M, Bolchini F C, Confalonieri L, Haddad F, Nigron E, Groppi F and Manenti S 2024 Experimental cross-section measurement of the nuclear reactions induced by protons on ^{159}Tb: Evaluation of the ^{155}Dy/^{155}Tb precursor system *Radiat. Phys. Chem.* **224** 112069
[32] Koning A and Rochman D 2012 Modern nuclear data evaluation with the TALYS code system *Nucl. Data Sheets* **113** 2841–934 special Issue on Nuclear Reaction Data
[33] Koning A, Hilaire S and Goriely S 2023 TALYS: modeling of nuclear reactions *Eur. Phys. J. A* **59** 131
[34] Gilmore G R 2008 *Statistics of Counting* (Wiley) pp 101–29
[35] Lau J C F and Hogan J J 1973 Investigation of branching ratios between isomeric states of ^{154}Tb *Phys. Rev. C* **8** 715–7
[36] IAEA, Live Chart of Nuclides - Advanced version, accessed: 2025-01-17, https://www-nds.IAEA.org/relnsd/vcharthtml/VChartHTML.html
[37] Bak L M, Nedovesov V G, Khol'nov Y V and Shchukin G 1973 Intensity of the isomeric transition of ^{154}Tb *Izv. akad. nauk SSSR ser. fiz.,* **37** 38–42 https://api.semanticscholar.org/CorpusID:102208465
[38] Kondev F, Wang M, Huang W, Naimi S and Audi G 2021 The NUBASE2020 evaluation of nuclear physics properties *Chin. Phys.* C **45** 030001
[39] Gyürky G, Rastrepina G, Elekes Z, Farkas J, Fülöp Z, Kiss G, Somorjai E and Szücs T 2009 Precise half-life measurement of the 10 h isomer in 154Tb *Nucl. Phys. A* **828** 1–8
[40] Gyürky G *et al* 2010 Alpha-induced reaction cross section measurements on ^{151}Eu for the astrophysical γ-process *J. Phys. G: Nucl. Part. Phys.* **37** 115201
[41] Otuka N and Takács S 2015 Definitions of radioisotope thick target yields *Radiochim. Acta* **103** 1–6
[42] Deb K, Pratap A, Agarwal S and Meyarivan T 2002 A fast and elitist multiobjective genetic algorithm: NSGA-II *IEEE Trans. Evol. Comput.* **6** 182–97
[43] Blank J and Deb K 2020 Pymoo: multi-objective optimization in python *IEEE Access* **8** 89497–509
[44] Feng Y and Zalutsky M R 2021 Production, purification and availability of ^{211}At: Near term steps towards global access *Nucl. Med. Biol.* **100-101** 12–23
[45] Kazakov A G, Aliev R A, Bodrov A Y, Priselkova A B and Kalmykov S N 2018 Separation of radioisotopes of terbium from a europium target irradiated by 27 Mev α-particles *Radiochim. Acta* **106** 135–40